

# Structure and dynamics of the nightside poleward boundary: Sounding rocket and ground-based observations of auroral electron precipitation in a rayed curtain

K. A. Lynch,<sup>1</sup> D. Hampton,<sup>2</sup> M. Mella,<sup>1</sup> Binzheng Zhang,<sup>1</sup> H. Dahlgren,<sup>3</sup> M. Disbrow,<sup>4</sup> P. M. Kintner,<sup>5</sup> M. Lessard,<sup>6</sup> E. Lundberg,<sup>5</sup> and H. C. Stenbaek-Nielsen<sup>2</sup>

Received 4 March 2012; revised 12 September 2012; accepted 21 September 2012; published 3 November 2012.

[1] The Cascades2 auroral sounding rocket provides a case study for comparing multipoint in situ ionospheric observations of a nightside auroral poleward boundary intensification with ground-based optical observations of the same event. Cascades2 was launched northward from Poker Flat Alaska on 20 March 2009 at 11:04 UT. The 13 min flight reached an apogee of 564 km over the northern coast of Alaska. The experiment included a five-payload array of in situ instrumentation, ground cameras at three different points under the trajectory, multiple ground magnetometers, the Poker Flat Incoherent Scatter Radar (PFISR) radar, and the Time History of Events and Macroscale Interactions during Substorms (THEMIS) spacecraft in the magnetotail. The rays of the poleward boundary intensification (PBI) curtain have along-arc motions of 8.5 km/s and along-arc spacings of 16 km. Modulated maximum energy envelopes and energy fluxes of the associated electron precipitation correspond to this spatial structure of the visible rays. The electron precipitation is additionally modulated at a higher frequency, and velocity dispersion analysis of these 8 Hz signatures implies Alfvénic wave-particle acceleration of an ambient ionospheric electron source occurring a few hundred km above the observation point. These observations parameterize the curtain of Alfvénic activity above the PBI event, both in the dispersive ionosphere and in the magnetotail reconnection region. The along-arc variations in brightness correspond to variations in precipitating electron energy flux interpreted as an along-arc modulation of the maximum energy of the Alfvénic wave-particle acceleration process; this is a new interpretation of the formation of rayed structures in auroral curtains. We consider the various possible magnetospheric and ionospheric drivers for the control of the observed along-arc structuring and motions.

**Citation:** Lynch, K. A., D. Hampton, M. Mella, B. Zhang, H. Dahlgren, M. Disbrow, P. M. Kintner, M. Lessard, E. Lundberg, and H. C. Stenbaek-Nielsen (2012), Structure and dynamics of the nightside poleward boundary: Sounding rocket and ground-based observations of auroral electron precipitation in a rayed curtain, *J. Geophys. Res.*, 117, A11202, doi:10.1029/2012JA017691.

## 1. Introduction: Poleward Boundary Aurora

[2] The nightside poleward boundary of the auroral oval has varied, structured, and dynamic electron precipitation

causing a variety of displays of visible aurora. Recent work has increased our understanding of visible ionospheric responses to interconnected magnetospheric and ionospheric activity. The Time History of Events and Macroscale Interactions during Substorms (THEMIS) array and its ground-based observatories have explored substorm development [Angelopoulos, 2008; Keiling *et al.*, 2008; Frisell *et al.*, 2011]. The REIMEI spacecraft with its on-board imager in conjunction with in situ particle measurements has shown examples of ionospheric response to U-shaped potentials [Asamura *et al.*, 2009] and ionospheric motions [Chaston *et al.*, 2010], as well as fine structure of black aurora [Obuchi *et al.*, 2011]. Ground-based camera and radar array studies have explored the relative timing and sequencing of ionospheric signatures of magnetospheric configurations [Rae *et al.*, 2010; Zesta *et al.*, 2002; Zou *et al.*, 2009].

[3] One striking feature of nightside aurora, particularly evident during solar minimum, is the poleward boundary intensification (PBI) curtain of Alfvénic rayed structures [Zesta *et al.*, 2006; Semeter *et al.*, 2005; Mella *et al.*, 2011].

<sup>1</sup>Department of Physics and Astronomy, Dartmouth College, Hanover, New Hampshire, USA.

<sup>2</sup>Geophysical Institute, University of Alaska Fairbanks, Fairbanks, Alaska, USA.

<sup>3</sup>Center for Space Physics, Boston University, Boston, Massachusetts, USA.

<sup>4</sup>NSROC, NASA/WFF, Wallops Island, Virginia, USA.

<sup>5</sup>School of Electrical and Computer Engineering, Cornell University, Ithaca, New York, USA.

<sup>6</sup>Space Science Center, University of New Hampshire, Durham, New Hampshire, USA.

Corresponding author: K. A. Lynch, Department of Physics and Astronomy, Dartmouth College, 6127 Wilder Lab, Hanover, NH 03755, USA. (kal@dartmouth.edu)

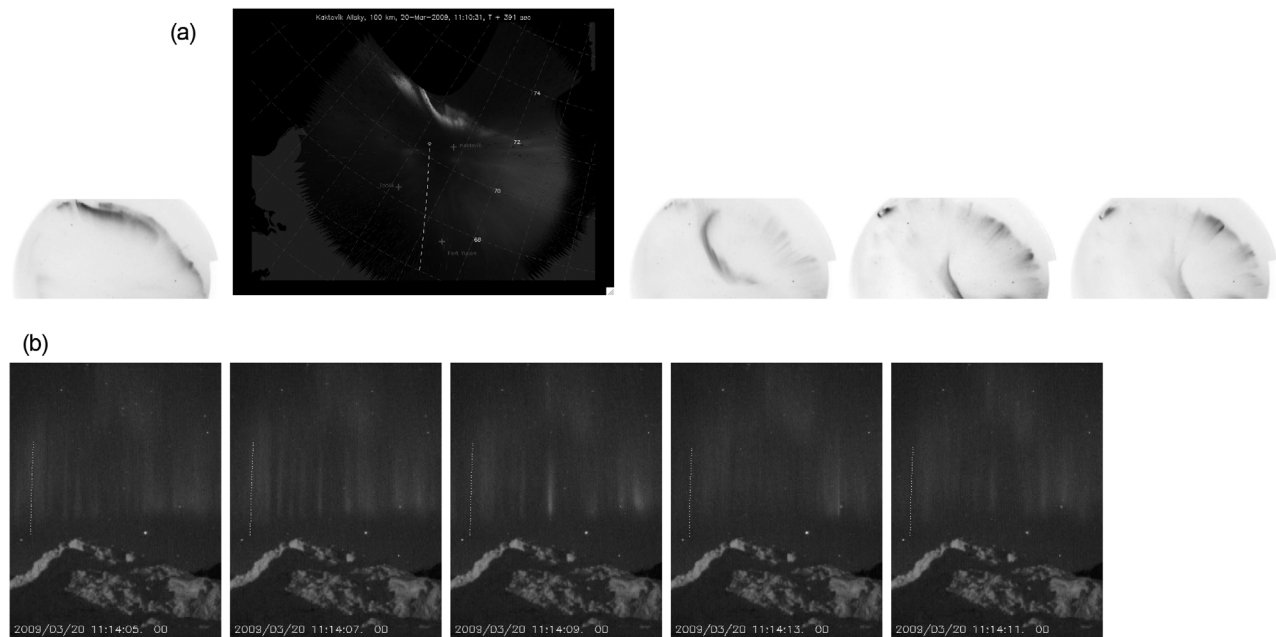


**Figure 1.** (a) Several views of the PBI curtain, from the Kaktovik all-sky camera. The second panel has been mapped to a geographic grid and also shows the ionospheric footprint of the payload's northward trajectory. From top to bottom, the auroral activity at 11:10:10 UT, 11:10:31 UT, 11:12:20 UT, 11:14:13 UT, and 11:14:30 UT; these times correspond to flight times  $T + 370$  s,  $T + 391$  s,  $T + 500$  s,  $T + 613$  s, and  $T + 630$  s. (b) A sequence of five views from the Toolik narrow field "guppy" camera, at  $T + 605$ ,  $607$ ,  $609$ ,  $611$ , and  $613$  s.

Figure 1 shows one such example. The proper interpretation of this visible structure as a dynamic probe of magnetospheric and/or ionospheric processes could be very valuable.

[4] Many previous studies have statistically parameterized auroral electron precipitation spectra, spatial scales, and temporal variations [Paschmann *et al.*, 2003; Newell *et al.*, 2009]. Ground-based optical studies have quantified the observed temporal and spatial scales of the visible and UV aurora [Borovsky, 1993; Trondsen and Cogger, 1998; Partamies *et al.*, 2010]. However, with the exception of recent REIMEI studies [Asamura *et al.*, 2009; Chaston *et al.*, 2010], observations which can explicitly relate optical aurora to in situ measurements of ionospheric precipitation have been rare [Wygant *et al.*, 2000; Stenbaek-Nielsen *et al.*, 1998] and mostly limited to all-sky camera fields of view with a spatial resolution of the order of a kilometer at best; certainly all of them, including REIMEI, are single-point in situ observations [Samara *et al.*, 2010]. One multipoint electron precipitation study, a sounding rocket named Auroral Turbulence 2 [Lynch *et al.*, 1999; Ivchenko *et al.*, 1999] was done in cloudy skies. Another multipoint electron precipitation study, the ROPA (Rocket Observations of Pulsating Aurora) pulsating aurora mission, was limited by high-voltage problems to 30–60 s of multipoint data [Jones *et al.*, 2008].

[5] The elements of converting from specified precipitating electron spectra to visible signatures are well understood and quantitatively modeled as sums of Gaussians [Lummerzheim and Liliensten, 1994]. However, most in situ ionospheric electron precipitation observations are single-track snapshots with little information about the time evolution or history of

the electron precipitation behavior. Since there are multiple precipitation spectra and histories which can lead to qualitatively similar visible signatures, it is difficult to invert interesting ground-based optical signatures into a map of the ionospheric precipitation with sufficient accuracy to constrain models of auroral dynamics [Zettergren *et al.*, 2010]. Recent work with the REIMEI spacecraft [Asamura *et al.*, 2009; Chaston *et al.*, 2011] has combined on-board field-aligned camera views of inverted-V events with electron precipitation measurements to put single-spacecraft in situ data in the context of evolving optical flow fields.

[6] The example shown in Figure 1 is part of a larger PBI event [Mella *et al.*, 2011]. Extensive literature relates PBI activity on large scales to intermittent tail reconnection and bursty flows [Lyons *et al.*, 1999; Zesta *et al.*, 2002, 2006]; Zesta *et al.* [2002] in particular relate PBI activity to shear flows in the flanks of the magnetotail. Mella *et al.* [2011] show that the PBI of Figure 1 is seen as part of an activation sequence lasting an hour. The Cascades2 rocket traversed both the streamer seen near zenith in the latter three images, and the poleward curtain seen in all the images. The in situ electron signatures observed were seen to be very different in the two cases, with a combined plasma sheet and ionospheric source for the streamer, and a purely ionospheric source for the poleward curtain. It is this poleward curtain which is the subject of this paper.

[7] A substantial literature relates Alfvénic Poynting flux into ionospheric PBI signatures to the braking of ion flows from reconnection events in the tail [Angelopoulos *et al.*, 2002; Mella *et al.*, 2011; Zesta *et al.*, 2006; Lyons *et al.*,

1999]. *Semeter et al.* [2005], *Lyons et al.* [1999], and *Mella et al.* [2011] all show evidence that ionospheric PBI signatures involve soft precipitation. More recent work on three-dimensional reconnection modeling also indicates a more direct source of Alfvénic Poynting flux, directly from the reconnection region [*Shay et al.*, 2011], in addition to the Alfvénic power generated by the braking of earthward ion flows. In either case, the principal energy driver for PBI signatures appears to be tail reconnection.

[8] Here we turn to the along-arc fine-scale structuring of the PBI event. We consider two possible controls for the observed structure and dynamics. Ionospheric instabilities such as the tearing mode instability [*Seyler*, 1988, 1990; *Wu and Seyler*, 2003; *Chaston and Seki*, 2010] have been shown in modeling work to create repeated quadrupolar structures along a current-sheet-defined arc. The growth rate of structure in the along-arc direction is governed by the initial thickness of the current sheet, with vortices forming at spatial scales along the arc of 1 to 1.3 times the width (C. C. Chaston, personal communication, 2012). Near the center of each of these structures, the Alfvénic activity is more dispersive (that is, it has a larger  $k_{\perp}$ ), the related parallel electric field is stronger, and the associated field-aligned electron acceleration is stronger, than between each structure, forming a series of electron precipitation enhancements, or rays, along the curtain. Since the Alfvénic acceleration of the electrons is broad in energy, the resulting visible structures are extended in altitude, giving a rayed appearance. The relationship between these dispersive Alfvén wavefields, and the associated electron acceleration, is well documented [*Kletzing*, 1994; *Lysak and Song*, 2005; *Watt et al.*, 2005; *Chaston et al.*, 2003; *Hui and Seyler*, 1992; *Seyler and Liu*, 2007]. It is these interactions which form the “Alfvénic aurora” and give the visible aurora such striking dynamics.

[9] The second interesting control of the observed structure is that imposed by large-scale flows, leading to regular along-arc motions in which the Alfvénic structure (both the higher altitude Alfvénic activity and the resulting electron precipitation) is entrained. Similar considerations have been examined for inverted-V arcs [*Asamura et al.*, 2009; *Chaston et al.*, 2011], comparing along-arc flow signatures as seen in the REIMEI camera with in situ inverted-V electron signatures. Here however we will present similar organized along-arc motions, but without the inverted-V quasi-static electron acceleration signature. The relationship between the large-scale flows, and the Alfvénic behavior which they organize, is unclear. A substantial literature, detailed above, describes both the Alfvénic acceleration process and the magnetotail bursty bulk flow processes which lead to PBI class Alfvénic structures. Another set of literature describes large-scale ionospheric flows and their relationships to auroral discrete arcs. The intersection of these two processes results in interesting and organized motions of Alfvénic accelerated structures. This coupling presents an interesting open question which is just beginning to be studied theoretically [*Chaston et al.*, 2011], and we present this Cascades2 event as a case study example.

[10] The Cascades2 auroral sounding rocket was designed as a case study for comparing multipoint in situ ionospheric observations of a nightside auroral event with ground-based

optical studies of the same event. Fortunately our launch event coincided with a near conjunction with three of the THEMIS spacecraft, allowing us to put the event into a magnetospheric context. The event consisted of a sequence of repeated poleward boundary intensifications (PBIs) [*Lyons et al.*, 1999] with intense Alfvénic activity defining the poleward edge of the oval. In this paper we detail the fine structure of the poleward boundary electron precipitation and compare it to simultaneous two-point narrow-field camera observations of the resulting visible auroral structures. A forthcoming work will detail the field measurements of this event. The resulting picture provides a case study of a rayed PBI curtain and the spatially and temporally variable Alfvénic processes above it.

[11] In section 2 we describe the mission and instrumentation, both in situ and ground based. Section 3 details the event itself on 20 March 2009 and the observed parameters of the structuring and dynamics. Section 4 introduces an interpretation of the PBI curtain consistent with the observed parameterization. Section 5 discusses the resulting picture and considers the feasibility of various controls for these parameters, both magnetospheric and ionospheric. Section 6 lists conclusions and open questions.

## 2. Methods and Instrumentation: The Cascades2 Sounding Rocket Mission

[12] The Cascades2 sounding rocket mission was launched northward from the Poker Flat Research Range in central Alaska on 20 March 2009 at 11:04 UT (roughly 30 min pre-midnight magnetic local time). The 12 min 43 s flight reached an apogee of 564 km over the northern coast of Alaska at 11:11:11 UT, and left the auroral oval at 11:14:40 UT before atmospheric reentry at 11:16:42 UT. The experiment array design was chosen to address questions about (1) shears in ionospheric electric fields and their ability to drive waves [*Lundberg et al.*, 2012a, 2012b]; (2) proper motion of auroral structures with respect to the ambient ionosphere (this paper); and (3) quantifying parameters of dispersive Alfvén wave phenomena and their effects on auroral flux tubes.

[13] Figure 2 shows the in situ five-payload array trajectory and relative positions, and the auroral activity during the poleward boundary event under study here. The trajectory reached apogee over the northern coast of Alaska; three of the five THEMIS payloads had ionospheric footprints near the upleg, shown with icons in Figure 2a. The Cascades2 in situ ionospheric measurements were made by instrumentation carried on five separate payloads launched from a single four-stage Black Brant XII launch. Two electric field sub-payloads (“subs”) were deployed axially from the central main payload; two smaller particle-free flyers (PFFs) were deployed perpendicular to the spin axis; the main payload spin axis was aligned to the magnetic field at T + 380 s flight time, and diverged from this alignment as the payload moved northward by approximately 2° per 100 s. The auroral activity as mapped with the stereo ground imaging is shown in Figure 2c. Using narrow field cameras at both Kaktovik and Toolik (described below), the locations of individual ray structures were mapped using stereo imaging. The black dots in the mapping illustrate individual visible structures

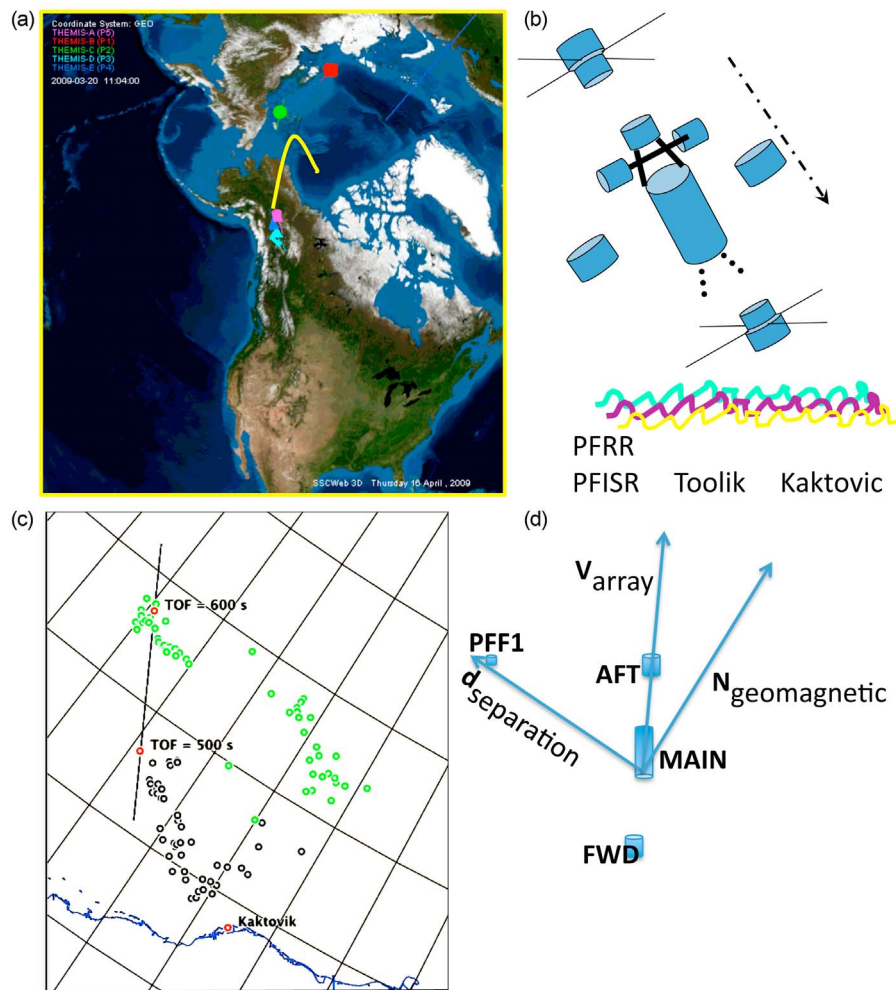


**Figure 2.** (a) A map of the trajectory in yellow, with THEMIS and Cluster2 footprints. (b) A cartoon of the five-payload Cascades2 array. (c) Geomagnetic mapping of the position of the array at times  $T + 500$  s and  $T + 600$  s, together with stereo-mapped locations of visible rays from times near  $T + 500$  s event (black dots) and times near  $T + 600$  s (green dots). (d) Projection of payload array relative positions into the perpendicular to  $\mathbf{B}$  plane.

seen near  $T + 500$  s flight time, corresponding to the streamer in the azimuth of the all-sky images of Figure 1a. The green dots illustrate the individual rays of the PBI curtain under study here, during the time when the payload crossed through the poleward boundary of the activity, near  $T + 600$  s flight time (the poleward curtain of Figure 1). This PBI activity is roughly aligned east–west in geomagnetic coordinates, extending in a curtain oriented  $59.5^\circ$  from the geographically northward trajectory.

[14] Figure 2d indicates the relative positions of the five-payload in situ array in the perpendicular to  $\mathbf{B}$  plane. The geometry is such that the main payload and particle-free flyer 1 (PFF1) enter the PBI curtain activity side by side (along a line parallel to the activity boundary) within 0.1 s of each other in the perpendicular to  $\mathbf{B}$  plane. At  $T + 450$  s (450 s after launch) the main-PFF1 separation vector is  $41.5^\circ$  west of the near-northward trajectory vector in the perp- $\mathbf{B}$  plane; at  $T + 700$  s it is  $39.9^\circ$  west; at  $T + 600$  s the two payloads are 866 m apart in the perp- $\mathbf{B}$  plane. The perpendicular to

$\mathbf{B}$  plane positions of the main payload and the two electric field subpayloads (“forward” and “aft” with the aft payload furthest northward; these payloads are so named because of their positions on the main payload during launch) closely follow each other (within  $10^\circ$ ) along the line of the trajectory. Thus motions of electron precipitation along the arc would be distinguished between the main and PFF1, while the motion of the array northward through the structure is apparent between the aft, main, and forward signatures. The high-cadence  $\mathbf{E}$  data on the subs show delays between signatures on the two subs caused either by motion along or across the arc [see *Lundberg et al.*, 2012a, 2012b]; the delays are interpreted as along-arc motion. PFF2, which was to provide a third point for the electron distribution function observations, suffered a deployment failure which destroyed the high voltage on that payload. Its magnetometer and GPS data are available.

[15] Each of the five payloads has GPS timing and position data to enable difference measurements between the

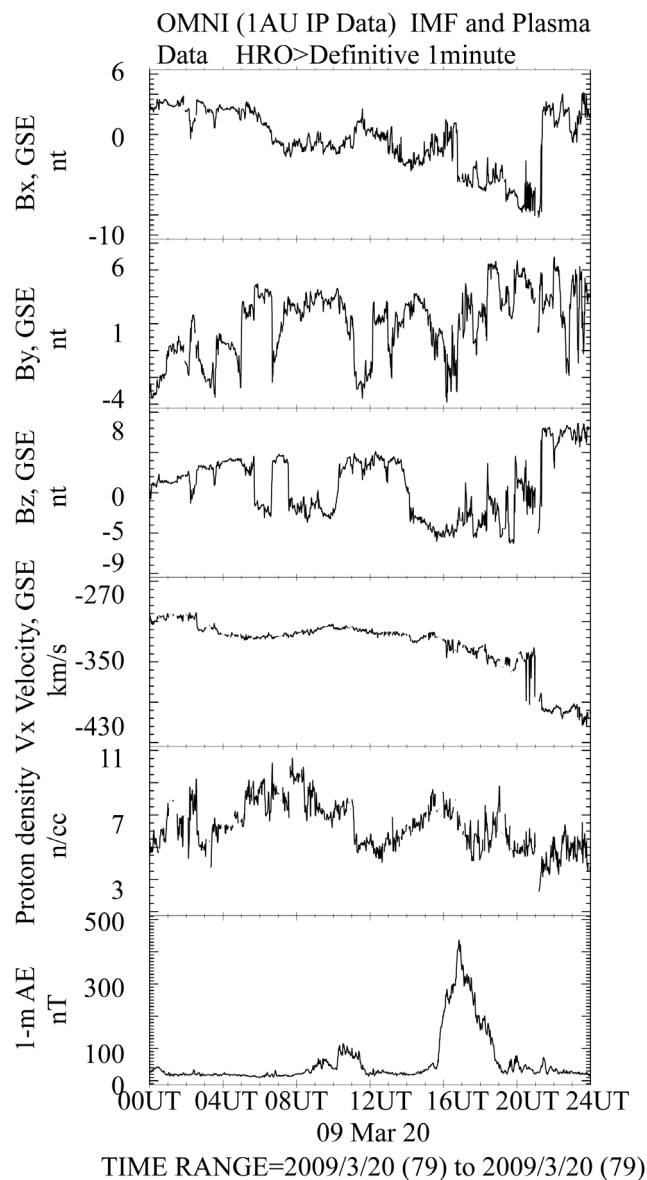


**Figure 3.** ACE and AE data from CDAW Omni Web site; 24 h of 20 March 2009. Data providers are J. H. King and N. Papatashvilli at AdnetSystems, NASA GSFC and CDAWeb.

observation points. Thus the resolution of the differences is given by the cadence of the different data types. For the primary electron distribution function measurements [Carlson *et al.*, 1983; Arnoldy *et al.*, 1999], there are 62.5 ms per energy sweep (up to 5875 eV) on the main and PFF1, with a phasing delay (unintended) of 32 ms between the two sweeps. The high-speed field-aligned electron detector [Mella *et al.*, 2011] on the main payload has a sweep rate of 8 ms per sweep (up to 1856 eV). The two subpayloads provide a flux measurement of all electrons above 3 eV at 125 ms cadence. Thus comparisons of integrated electron flux along the trajectory can be made at 125 ms resolution. Comparisons along the length of the arc between the main and PFF1 can be made at 62 ms resolution. At the time under study (600 s flight time), the separation of the main and the

PFF1 in the perpendicular to **B** plane is 866 m. The separation of each of the subpayloads from the main along the trajectory in the perpendicular to **B** plane is 254 m (forward) and 235 m (aft), and the northward velocity of the entire array is 1500 m/s.

[16] Standard monitoring cameras provided by UAF/GI at Poker Flat (PKR, 65.119°N, 147.432°W), Kaktovik (KAK, 70.133°N, 143.633°W), and Toolik Field Station (TOO, 68.627°N, 149.594°W) (geographic coordinates), and additional campaign-specific narrow field imagers were operated at TOO and KAK during the rocket flight. At KAK a white-light all-sky video camera and a narrow field intensified CCD (ICCD) camera both operated at 30 frames per second. The ICCD was filtered with a magenta filter to suppress the long-lived 557.7 and 630.0 nm emissions, collecting primarily N<sub>2</sub> first-positive (1P) and N<sub>2</sub><sup>+</sup> first negative emissions, both of which are prompt emission. The ICCD field of view was 20°, by 16°. At TOO a digital all-sky camera collected images every 5 s, and a narrow field CCD (NCCD) with a 24°, by 33°, field of view collected images through a 645 nm long-pass filter (collecting primarily N<sub>2</sub><sup>+</sup> emissions) at 2 fps (frames per second).

[17] Other ground-based data available to our study include multiple magnetometer chains in Canada and Alaska, and the Poker Flat Incoherent Scatter Radar (PFISR) radar at Poker Flat Research Range (data described by Mella *et al.* [2011]).

### 3. Observations

[18] Figure 3 shows the larger context of our event. A small dipolarization (seen on the THEMIS-E spacecraft FGS (fluxgate magnetometer sensor)  $B_z$  channel, not shown here) possibly resulted from a northward turning of IMF  $B_z$  just after 10:00 UT;  $B_z$  remained northward throughout the PBI interval, with a fairly strong negative  $B_y$ .  $K_p$  remained below 1 throughout the interval; the dipolarization and resulting small substorm at 10:30 UT caused a small increase in AE from 10:30 to 11:30 UT.

#### 3.1. Camera Data

[19] Figure 1a shows the all-sky camera view of the PBI event. The poleward curtain was evident north of Kaktovik from before 10:30 UT through 11:30 UT. Midway through the flight time, a streamer pulled equatorward from the poleward curtain, crossing the rocket trajectory near T + 475 s flight time. Figure 1b shows a representative sample of the curtain evolution as viewed from the south at Toolik station. Bright rapidly moving rayed structures moved in both directions along the poleward edge.

[20] Figure 4 shows a higher temporal resolution keogram of the poleward rayed arc from images collected at 30 fps by the ICCD camera at Kaktovik. The keogram was created by rotating each image so that the magnetic field lines are aligned along image columns and averaging the signal from fifty rows to improve the signal-to-noise ratio for each column. The azimuth of the camera is centered on 340°, geographic, with east to the right. At this azimuth the optical axis intersects the arc at 72°, geomagnetic latitude at a range of 280 km and at a 45°, angle. The time ranges from 11:13:43 UT (T + 583 s) to 11:14:13 UT (T + 613 s) during

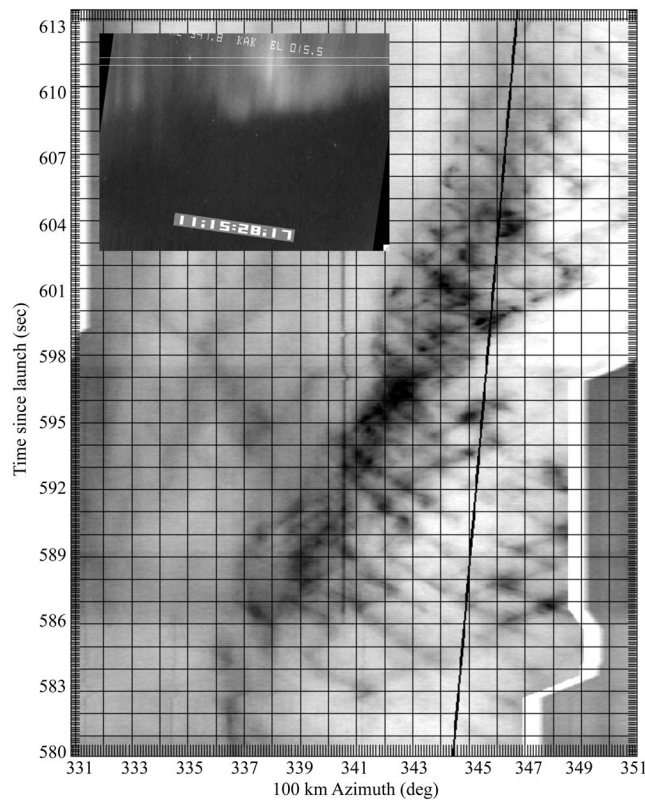


**Figure 4.** (inset) Example still from the Kaktovik narrow field camera; image shows the rotated to field-aligned image and the altitude limits of the integration for the keogram. Main image is Keogram (reversed color scale) of narrow field slices from T + 581 s through T + 613 s. The solid black line shows the position of the payload footprint with time (vertical axis) and azimuthal field of view (horizontal axis).

which time the on-board electron sensors were measuring significant field-aligned precipitation.

[21] Presented in this manner the progression of auroral emissions is seen to be quasiperiodic and bidirectional. The motion is evident in the keogram as a series of intensifications each lasting about 1 s, with a series of intensifications progressing at regular spatial and temporal intervals. Typically a series is composed of five intensifications, traveling as far as  $8^\circ$  in azimuth, or 56 km, before either exiting the camera field of view to the east or reaching the end of the emission region to the west. A sample of a dozen of these structures shows that the average spacing is  $16 \pm 2.8$  km. The average motion is  $1.3^\circ/\text{s}$ , which at 280 km range and compensating for the  $45^\circ$ , foreshortening corresponds to  $8.5 \pm 0.5$  km/s. Both the spacing and speed are the same for either direction of motion. With this ray speed and separation, at any one azimuth the periodicity of associated electron precipitation should be  $\sim 2$  s. A similar 2 s periodicity is seen in the in situ particle data, as we will see below. Peaks in intensity generally, but not exclusively, occur when rays traveling in opposite directions coincide. Distinct rays are often discernible in individual images, especially when they correspond to intensifications in the keogram. When an individual ray can be isolated the width of the ray can be as

small as 1 km, and when two rays intersect the resulting region of emissions broadens to as much as 4.5 km.

### 3.2. In Situ Electron Data

[22] Figure 5 shows the in situ electric field data, electron differential energy flux spectra, and integrated energy flux moment, during the crossing of the main payload and PFF1 through the principal region of Alfvénic activity near T + 600 s. Figure 6 shows a higher time resolution view of the precipitation as seen by the field-line-looking Bagel instrument on the main payload. As shown by *Mella et al.* [2011], the precipitation during this event is highly field aligned. Note that the PFF1 payload was not well field aligned; since the precipitation is highly field aligned, the PFF1 has an intermittent view of the precipitation as the PFF1 payload spins and cones.

[23] At this time the payload array is at an altitude of 450.4 km and is moving  $3^\circ$  east of northward in the perp-B plane at 1500 m/s. Parallax studies using the TOO and KAK camera data show this to be a 10 km meridionally wide region of geomagnetically eastward and westward moving rayed structures, apparently or nearly colocated based on the lower borders, and tomographic mapping, of the visible signatures. The electron data show a clear entrance into the activity at T + 586.5 s. The activity (electron precipitation energy and energy flux) weakens to a minimum at T + 597 s, and then increases sharply again at T + 600 s. The most intense activity lasts from T + 586 s to T + 615 s, a north–south width of 44 km; given the variation in energy flux across the event, this is consistent with the camera data (see discussion in section 5.4) Within the event, the rays slide sideways; the optical narrow field camera keograms indicate counter-moving structures along the rayed curtain. Note, importantly, that the payload moves northward at 1.5 km/s while the rays move along the arc at 8.5 km/s; thus much of the variation seen by the electron detectors within the precipitation region corresponds to along-arc rather than across-arc structure.

[24] We consider in particular two scales of structuring in these electron signatures. First, there is an energy flux modulation on scales comparable to the ray size, spacing, and velocity described just above in the camera data discussion. This modulation appears at a roughly 2 s cadence in the electron energy flux (i.e., at times T + 602.25 s, 604.5 s, 606.7 s, and 608.2 s on the main payload, as described in section 4). The camera-observed 8.5 km/s motion of the ray enhancements corresponds to a 0.1 s lag time between PFF1 and the main payload electron detectors, very close to the 62 ms cadence of the detector sweeps, making it difficult to pin down the respective electron signatures. The envelope lines in Figure 5 (top) outline the envelope of maximum electron acceleration energy; these envelopes, related to energy flux and to camera brightness, as discussed below, provide the best comparison between the main and PFF1 electron signatures. These electron structures in the T + 589 s event either hit both payloads together or hit the PFF1 first and then the main payload, consistent with eastward motion of  $0.866 \text{ km}/0.1 \text{ s}$  ( $=8 \text{ km/s}$ ) or faster. The small event at T + 595.5 s hits the PFF1 first, with a larger time delay. The entrance structure at T + 600 s hits the PFF1 0.1 s before the main ( $8 \text{ km/s}$  eastward motion). To the resolution of the

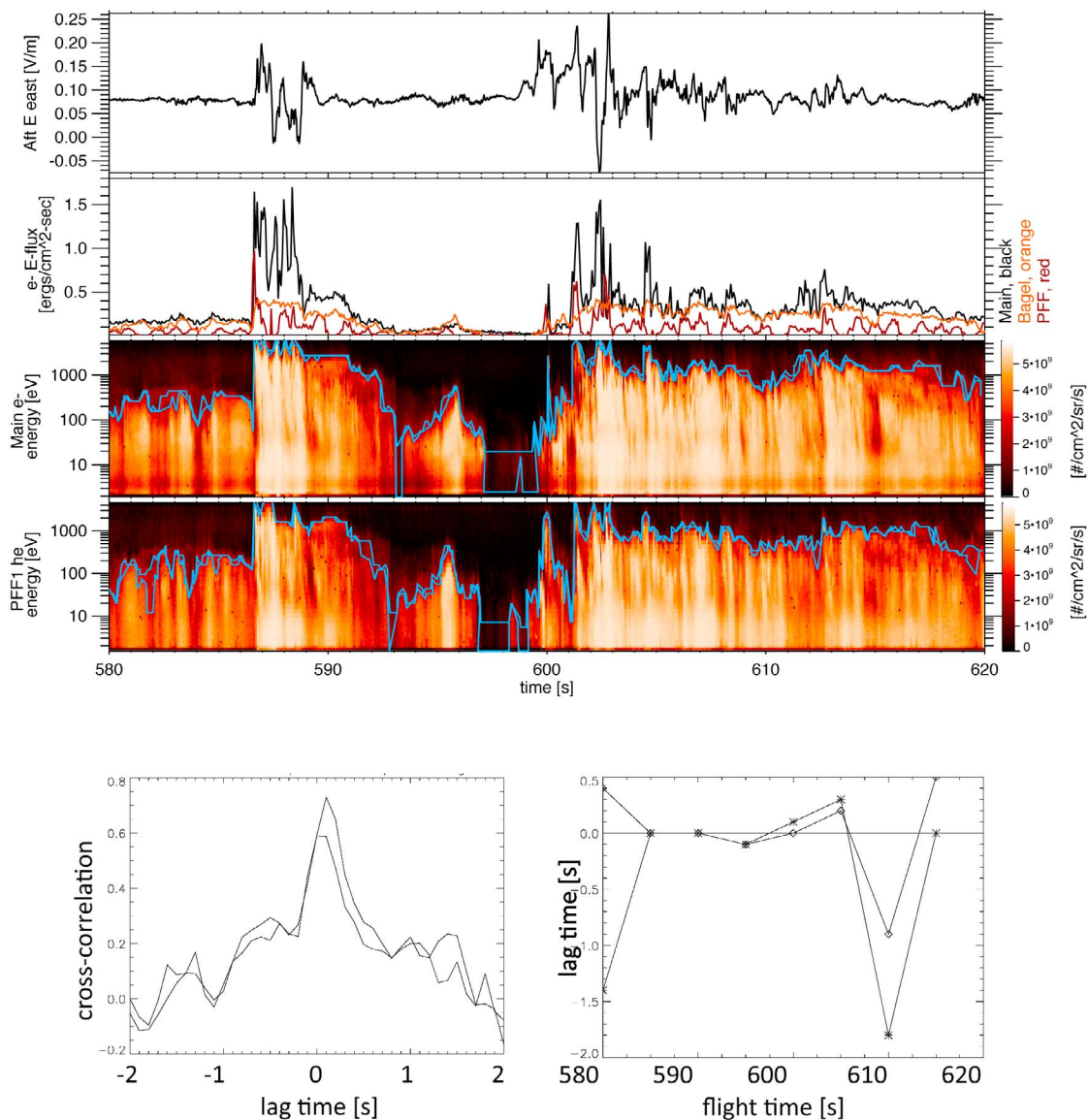


**Figure 5.** (top) For flight times from  $T + 580$  s to  $T + 620$  s, the top panel shows DC electric field data from the AFT subpayload. The second panel shows the integrated precipitating energy flux from the main payload and PFF1 electrostatic analyzers. The third panel shows the differential energy flux as seen on the main and the fourth the same from PFF1; the blue lines trace out the envelope of maximum acceleration energy. (bottom left) The cross correlation as a function of lag time between the maximum energies seen by the PFF1 and the main for the interval from  $T + 598$ – $T + 606$ ; and (bottom right) the dominant lag time for each 5 s interval from  $T + 580$  to  $T + 620$ . Positive lag times correspond to signatures hitting PFF1 first and main second. The two traces in each plot indicate the range of error in the analysis.

electron data cadences, these sideways propagation delays are consistent with the keogram ray velocities of 8 km/s.

[25] All of these electron signature delays indicate eastward propagation, to the limitation of the data cadences. Figure 5 (bottom) quantify these delays using correlation lag times between the maximum energy envelopes for the two payloads (we do not use the energy flux moments because of the intermittent view of the PFF1 sensor). The two traces in Figure 5 indicate the range of error in the analysis, which was done twice using independently extracted patterns for the maximum energy envelopes in the main and PFF1 spectrograms.

[26] Second, in addition to this structure corresponding to the camera view of the rays, there is an additional electron signature seen within and throughout the rayed curtain. This higher-cadence modulation is interpreted as a temporal signature (see section 4). It is best seen in Figure 6; only the higher-cadence, field-line-looking electron sensor sees this signature well. The spectrogram in Figure 6 (top) shows a blown-up view of the interval from  $T + 600$  to  $T + 610$  s. Nested sets of velocity-dispersed signatures are seen throughout the interval, in particular at high energies just after  $T + 602$  and at lower energies just after  $T + 606$  s and just after  $T + 608$  s. The repetition rate of these nested

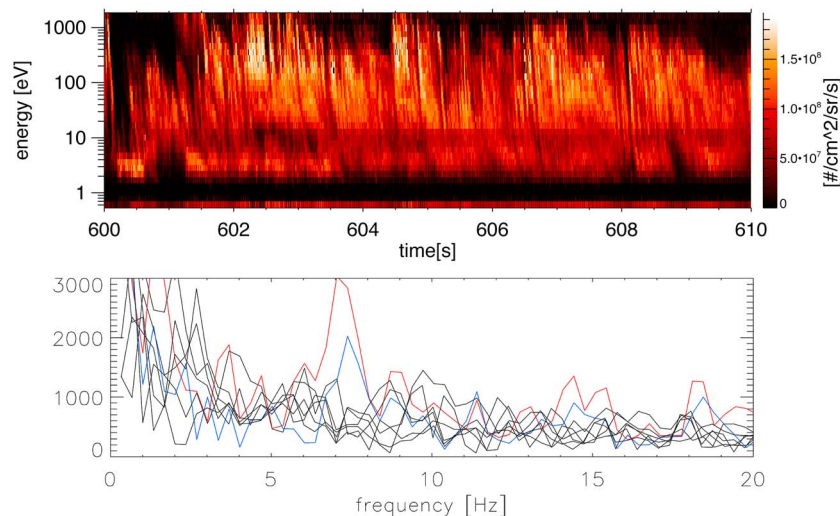


**Figure 6.** (top) For the shorter time interval from T + 600 s to T + 610 s, the differential energy flux spectra seen by the high-cadence field-line-looking Bagel electron detector. (bottom) FFTs of 3 s intervals of cuts through the spectrogram at energies 749–971 eV. The red FFT is from T + 601–604, and the blue one is from T + 602–605.

dispersion signatures is roughly 8 Hz. Figure 6 (bottom) shows Fourier transforms of a cut through the spectrogram at energies 749–971 eV. Each line is a Fourier transform of a 3 s window through the 10 s interval shown. At this energy cut, the nested dispersions are clearest between T + 602 and T + 604; the red fast Fourier transform (FFT) is from T + 601–604, and the blue one is from T + 602–605. The frequency peak is, for this example, between 7 and 8 Hz.

### 3.3. In Situ Magnetic Field Data

[27] Figure 7 shows a scalar measure of the angle between the main-payload-measured  $\mathbf{B}$  and the International Geomagnetic Reference Field (IGRF) model. (These data are found by subtraction from the observations of a rigid-body model rotation of the IGRF magnetic field vector into the payload frame, not by frequency-based filtering.) The value shown is simply the magnitude of the angular difference between the two vectors, and thus does not indicate the direction of this deflection, only its size. The increasing deflection from T + 475 s through T + 525 s coincides with passage through the precipitating electrons of the equatorward moving streamer shown in Figure 1. The decreasing deflection from T + 525 s through T + 675 s is consistent with northward passage through a large-scale east–west aligned current sheet. Of particular interest to our study is the localized enhancement near T + 600 s. This structure contains strong Alfvénic activity. The magnetometer data shown here shows the bulk structure of this event to have a width of approximately 10 km, from T + 597 s through T + 607 s, with embedded finer structure; the largest of these is from T + 600 s through T + 602.5 s. Note that at this time the payload is moving northward at a velocity of 1.5 km/s.

[28] A zeroth-order estimation of the field-aligned current sheets which could cause these deflections can be calculated by measuring the quantity  $\delta B / (L_{north})$  as an estimate for  $\nabla \times \mathbf{B}$ , assuming the payload to be crossing northward through an east–west aligned structure with variation only in

$\mathbf{B}_{east}$ . An angular deflection of  $10^{-3}$  rad of a magnetic field vector of 40,000 nT corresponds to a perpendicular magnetic field component of 40 nT. The large-scale structure from T + 525 through T + 675 (150 s of travel time so a northward distance of 225 km) has an overall deflection of  $6 \times 10^{-3}$  rad. This would correspond to a field-aligned current density of  $\frac{1}{\mu_0} * 40 \text{ nT} * 6 / (225 \times 10^3)$ , or  $0.8 \mu\text{A}/\text{m}^2$ . The smaller region intensification from T + 600 to T + 610 corresponds to a current density of order  $8.5 \mu\text{A}/\text{m}^2$ .

### 3.4. In Situ Thermal Electron Data

[29] Figure 8 shows the ambient ionospheric thermal electron temperature (measured by the Electron Retarding Potential Analyzer (ERPA) instrument) during the event under study, along with the pitch angle width of the field-aligned electron precipitation (measured by the top hat analyzer). The top hat electron detector which images pitch angle has 30 bins in a  $360^\circ$  2-D planar field of view. Since the field-aligned precipitation is seen in only one or two of these bins at any time, its perpendicular temperature (i.e., its source temperature) is (considerably) less than a few 10 s of eV. Furthermore, the perpendicular temperature of the field-aligned beam (as indicated by its pixel width) tracks the ambient population  $T_e$ , reinforcing the idea that the ionosphere is the local source of this precipitation (see discussion in section 5.2). The soft precipitation of the Alfvénic aurora has an extremely efficient transfer of energy to the background population [Lynch *et al.*, 2007] and the stationarity of the PBI curtain allows the ambient heating to build up [Semeter *et al.*, 2005].

## 4. Parameterization

[30] We can combine the above observations to gather a set of parameters for the PBI curtain. The keogram information says that the visible ray spacing is 16 km, the ray width is 2 km, and their propagation velocity is 8.5 km/s; these

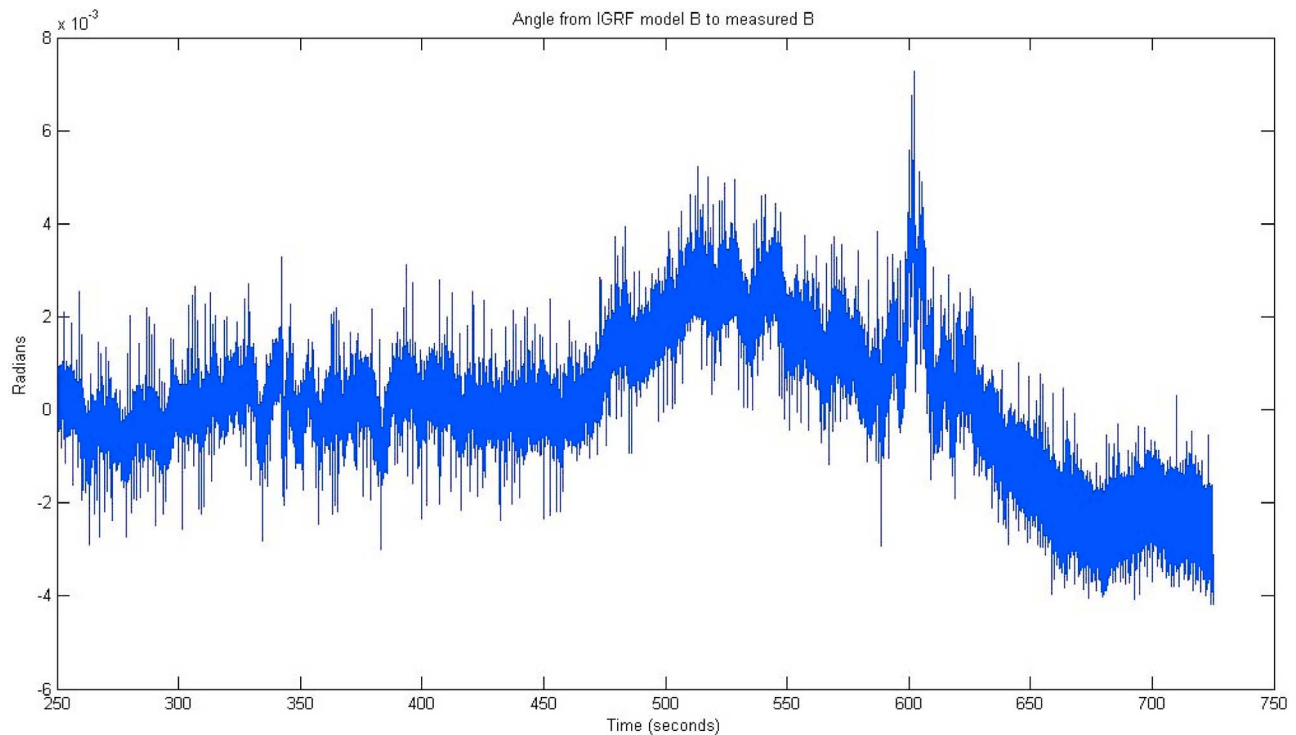


**Figure 7.** Angle between measured **B** and IGRF **B** as measured by the main payload deck-mounted Billingsley science fluxgate magnetometer.

rays would cross over the payloads with a 2 s intermittency. Figures 5 and 6 show many structures in the electron precipitation. The energy flux peaks (and associated increases in the maximum energy envelopes) at  $T + 602.25$  s, 604.5 s, 606.7 s, and 608.2 s have the appropriate spacing to match the observed visible rays. Also, there is clearly a higher-frequency time variability to the electron precipitation, as can most clearly be seen in the higher-cadence field-aligned electron data in Figure 6. The characteristic energy versus time dispersion curves within this modulated field-aligned precipitation are consistent with a localized broad energy acceleration of particles at distances from 120 to 300 km up the field line above the payload observation [Clemmons *et al.*, 1995; Lynch *et al.*, 1999]. In the discussion below, we interpret these various signatures as the result of an acceleration structure a few hundred kilometers above the rocket altitude, along the PBI curtain. This structure needs a modulated maximum energy of interaction (between the Alfvénic activity and the ambient electrons) with 16 km along-arc wavelength spatial structure and with an 8.5 km/s propagation velocity along the arc structure (the collection of rays), together with an overlaid 8 Hz temporal signature.

[31] In this picture, we consider the ray brightness, which is proportional to electron precipitation energy flux, to be controlled by the variable (along the curtain) maximum energy of the Alfvénic acceleration process. Energy flux can be increased by increasing the energy, or by increasing the flux; here we presume the control to be the maximum energy of interaction. The spacing and speed of the visible rays gives a spatial scale length and apparent phase velocity along the arc. Intensity enhancements correspond to energy

flux enhancements. The energy flux enhancements come from along-arc modulation of the maximum Alfvénic acceleration energy, and velocity dispersion of the resulting accelerated electrons gives the altitude of electron-wave interaction.

[32] A careful examination of the camera data shows the intensity level between the rays to be about 10–30% higher on average than the background. The set of enhancements

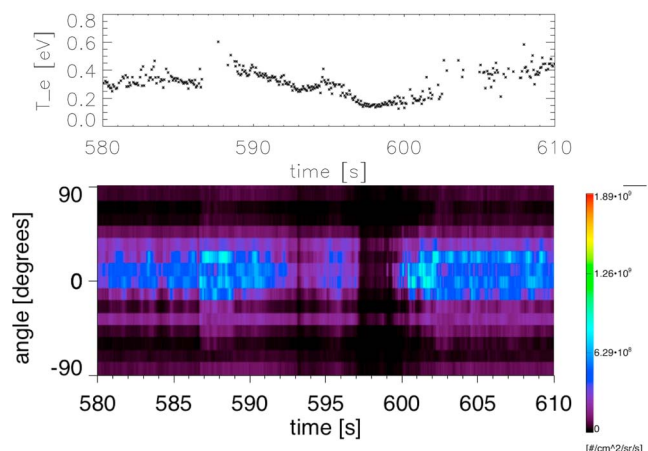


**Figure 8.** (top) Ambient electron temperature, measured by the ERPA instrument. (bottom) Pitch angle width of field-aligned electron precipitation, measured by the top hat electrostatic analyzer.

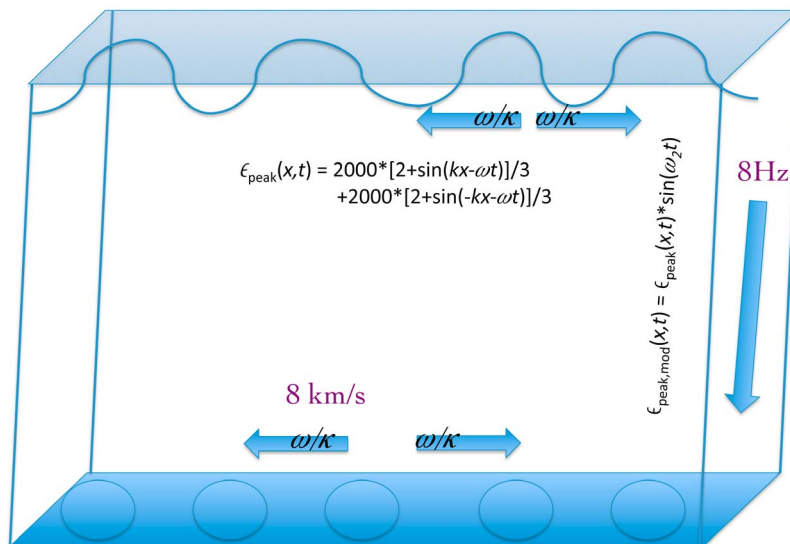


**Figure 9.** An illustration of the PBI curtain and the acceleration region above it. The curtain is extended in the east–west direction and consists of a series of rays, illustrated as circles at the bottom of the box. The rectangular box is 200 km tall, indicating the distance between the rocket observations at the bottom of the box and the Alfvénic acceleration process at the top. The rays move in either direction along the long dimension of the box, with an along-arc velocity  $\omega/k$  determined by the camera observations and by the intermittency in the observed electron energy flux.

moves in a correlated fashion (as a rayed arc), with peak intensities up to three times the inter-ray intensity. The associated electron precipitation signature also shows modulations, with variations in the maximum energy of 50 percent and up to 60 percent variations in energy flux. (Note that the PFF1 energy flux moment calculations, because of the intermittent view of the field line, tend to miss the peaks of the energy flux.) It is important to note that both the electron maximum energy signature, and the visible curtain, are consistent with a modulated curtain picture rather than a series of separated, individual events in a plane.

[33] We combine these parameterizations in the following discussion. Figure 9 illustrates a cartoon of the PBI curtain and the acceleration region above it.

[34] Consider a source of Alfvénic accelerated ionospheric electrons consistent with the observations from  $T + 600$  s to  $T + 610$  s. We begin by inferring the presence of a curtain of Alfvénic activity driven by reconnection in the tail (we discuss this fully in section 6). As this Alfvénic activity approaches the lower ionosphere, it becomes dispersive, in the sense of developing a  $\mathbf{k}_\perp$  and an  $\mathbf{E}_\parallel$ . The peak wavefield potential of this dispersive Alfvén wave (DAW) activity (which here is presumed to control the maximum electron energy envelope and energy flux and therefore auroral brightness) which accelerates the ionospheric source particles varies longitudinally (along the arc) with a 16 km wavelength and an 8.5 km/s structure velocity, thus passing by the observation point with an apparent 2 s intermittency. This motion is seen in the camera as brightness enhancements moving both eastward and westward along the arc. The camera data add all brightness along the line of sight. In the interpretation developed below, we say that the payload is either in a region of eastward moving or westward moving rays at a given time; and that the

groups of rays are nearly coplanar. The modulation of the maximum electron energy in the direction  $x$  along the curtain varies (because of the spatially varying peak DAW potential) from a maximum of 2 keV to a minimum of 660 eV:

$$\mathcal{E}_{\max}(x, t) = 2000 * [2 + \sin(kx - \omega t)] / 3 \quad (1)$$

where  $k = 2\pi/\lambda = 2\pi/16$  km,  $\omega = 2\pi/T = 2\pi/(2s)$ , and  $x$  represents distance along the arc. For rays moving in the other direction, the argument would change to  $(kx + \omega t)$ . Assume that a wave-particle interaction, between an Alfvén wave and the local thermal electron population, at a point 200 km up the field line above the observation point creates a flat spectrum of electrons up to this maximum energy at any given  $x$  and  $t$ . Then, in addition, there is a temporal variability to the source with the observed 8 Hz frequency:

$$\mathcal{E}_{\max, \text{modulated}}(x, t) = \mathcal{E}_{\max}(x, t) * \sin(\omega_2 t) \quad (2)$$

where  $\omega_2 = 2\pi/(0.125$  s). Only those  $(x, t)$  observation points for which  $\mathcal{E}_{\max, \text{modulated}}$  is positive are assumed to have electrons accelerated downward toward the rocket; the others are assumed to be accelerated up the field line by the wave-particle interaction. This creates a source population, with an assumed flat spectrum up to this modulated maximum energy  $\mathcal{E}_{\max}(x, t)$ , at each point  $(x, t)$ , 200 km above the payload. A simple dispersion analysis on each particle allows a representation of what would be seen at the payload as the measurement point moves northward across the west or eastward propagating structures, assuming no variation in  $y$  (the northward direction). The upper panel of Figure 10 shows a keogram of  $(\mathcal{E}_{\max, \text{modulated}}(x, t)^{(3/2)})$  above a threshold, in the same format as those of the narrow field camera data in Figure 4. The exponent of  $(3/2)$  is because brightness

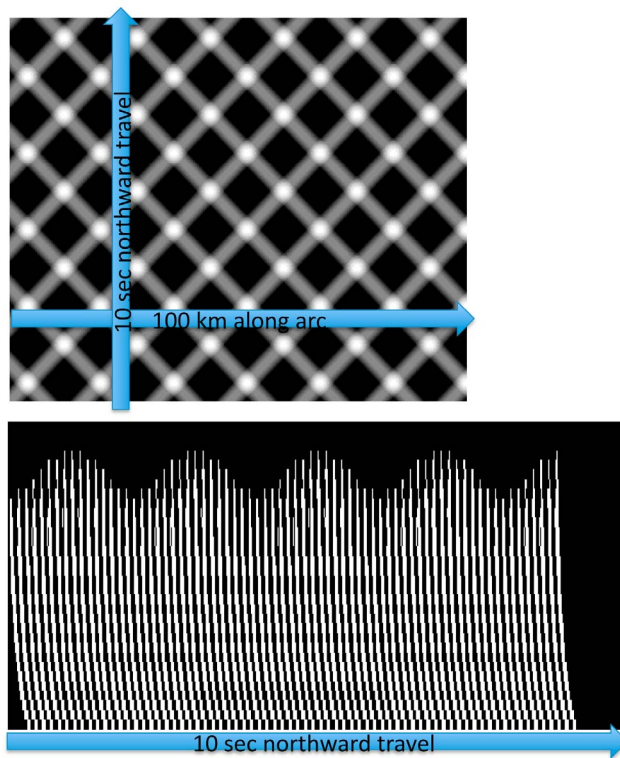


**Figure 10.** (top) A keogram generated from the interpretation described in the text, in the same format as Figure 4. (bottom) The resulting electron signatures seen at the rocket altitude, in the same format as Figure 6, illustrating both the modulation of the maximum energy and the 8 Hz periodicity of the dispersed bursts.

is proportional to energy flux; the threshold is because, roughly, there is an energy threshold for observable visible emissions. The keogram is 100 km wide and 10 s high. The payload moves northward across the structure at 1500 m/s, thus cutting a vertical line upward through the keogram. The lower panel shows the resulting electron energy spectrum at the payload, 200 km below the bottom of the acceleration region, with the observed features of the 2 s intermittency of the maximum energy, and the strong dispersion signature of the modulated precipitation at 8 Hz.

[35] The picture which thus emerges from the electron data is an east–west extended structure of DAW-thermal electron interactions, with a spatially structured peak electric potential of spatial wavelength 16 km, entrained in a background flow of 8.5 km/s, giving it an apparent 2 Hz signature, and separately, a true 8 Hz temporal frequency. The 8 Hz is here interpreted as a true temporal feature of the Alfvénic structure, consistent with the time-dispersive electron signatures. The apparent parallel phase velocity of the Alfvénic field activity from the source to the payload (as determined by the 0.128 s delay time between the onset of the field-aligned electron precipitation, and the onset of the electric field wave activity, at the  $T + 586$  s entry point) is 1600 km/s, consistent with field data estimations of the local Alfvén speed.

[36] Thus, in these electron data features we see that the 8 Hz temporal oscillation is indicative of the Alfvénic

interaction frequency, while the 2 s intermittency and the 16 km wavelength are artifacts of the spatial variation of the peak electric potential of the DAW interaction combined with ionospheric flows. The camera keogram, which integrates along the oblique line of sight, sees two nearly coplanar sheets of rays moving in both directions; the rocket payloads, moving across these adjacent sheets, are traversed by one sheet of rays at a given time.

## 5. Discussion

[37] We turn now to a discussion of what controls these observed parameters. We address in turn (1) the magnetospheric source of the Alfvénic Poynting flux; (2) the 8 Hz temporal structure within the rayed activity; (3) the 16 km spacing and 2 km size of the rays; and (4) the 8.5 km/s phase velocity of the rays.

### 5.1. Magnetospheric Alfvénic Poynting Flux

[38] Figure 11 shows the results of a 3-D Lyon-Fedder-Mobarry (LFM) global magnetospheric simulation [Lyon *et al.*, 2004] of the 20 March 2009 event, and a comparison to the ground-based all-sky camera meridian cut keogram. The LFM model was driven by the data shown in Figure 3 and illustrates nicely the original driving source of the Alfvénic Poynting flux of our event.

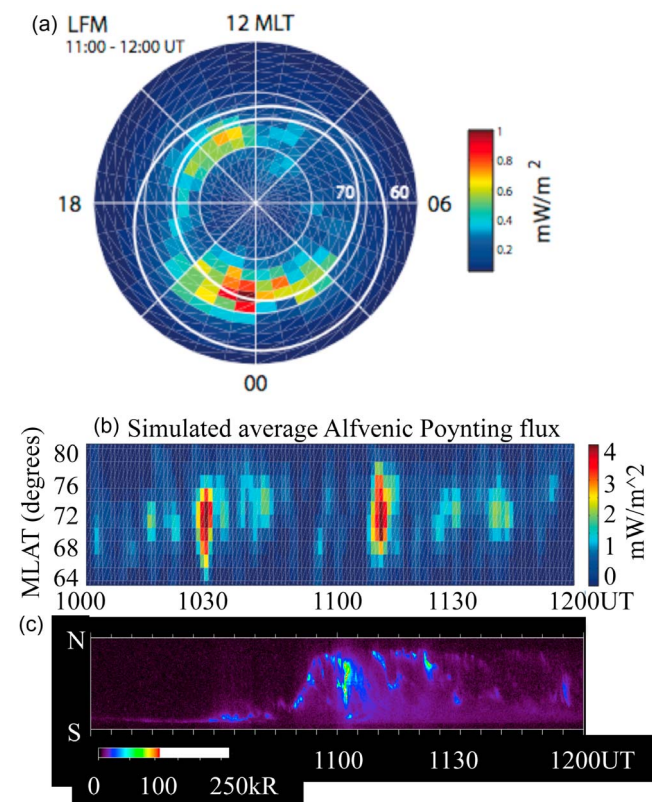


**Figure 11.** (a) Alfvénic Poynting flux through a  $6 R_E$  sphere as calculated using the LFM model driven by the data shown in Figure 3. (b and c) Temporal behavior of the Poynting flux as indicated by the model and by the ground camera data brightness.

[39] The simulated field-aligned Alfvénic Poynting flux  $S_{\parallel}$  is calculated as

$$S_{\parallel} = \frac{1}{\mu_0} \delta \mathbf{E} \times \delta \mathbf{B} \cdot \frac{\mathbf{B}}{B} \quad (3)$$

where  $\mu_0$  is the permeability of free space and  $\mathbf{B}$  is the mean vector magnetic field calculated from a 180 s running average of the locally measured magnetic field. Perturbation  $\delta \mathbf{E}$  and  $\delta \mathbf{B}$  were calculated by subtracting a 180 s running average of each measured field from 6 s averages of each field. The resulting Poynting flux values were then projected to a reference ionospheric altitude of 100 km by mapping  $S_{\parallel}/B = \text{const}$  along dipole magnetic field lines.

[40] The resulting distribution of average downward  $S_{\parallel}$  in the Northern Hemisphere between 11:00 UT to 12:00 UT, 20 March 2009 from the LFM simulation is shown in Figure 11a. The average Alfvénic Poynting fluxes exhibit two main regions of enhanced intensity. The dayside enhancement occurs between 13:00 and 15:00 MLT and  $76^\circ$  and  $80^\circ$  MLAT. The nightside enhancement occurs between 22:00 to 24:00 UT and  $68^\circ$  and  $76^\circ$  MLAT. In the MHD simulation, the dayside Alfvénic activity near the cusp region is a consequence of the time varying upstream driving conditions while the nightside Alfvénic power originates from the dynamic plasma and electromagnetic processes in the magnetotail. *Zhang et al.* [2012] show that in the LFM simulation, both fast and shear modes are generated in the equatorial plasma sheet region through the braking of fast earthward plasma flows (near  $x_{SM} = -15 R_E$ ) which originate from reconnection process in the magnetotail. As the wave power propagates from the plasma sheet to low altitude ( $6 R_E$ ), the fast mode wave power decreases rapidly due to isotropic propagation and the simulated  $S_{\parallel}$  is basically Alfvénic.

[41] The time variation of average  $S_{\parallel}$  in the premidnight sector (from 22:00 to 24:00 UT) is shown in Figure 11b, and can be compared to the ground camera brightness in the same format in Figure 11c. We look for relationships between downward Alfvénic Poynting flux and soft precipitation signatures. The simulation results show that from 11:10 to 11:55 UT, periodic large-scale Alfvénic Poynting fluxes generated in the magnetotail flow into the premidnight sector of the ionosphere between  $66^\circ$  and  $76^\circ$  MLAT, with a time period of roughly 15 min, which is similar to the temporal variation of auroral brightness observed by the ground camera. That the temporal variations are similar is somewhat surprising because the dispersive Alfvén waves are subgrid in the simulation, and because the physics of dispersive Alfvén waves are not included in LFM simulation. Two noteworthy differences between the ground camera observation and simulation results are as follows.

[42] First, there is an approximately 10 min lag between the simulated  $S_{\parallel}$  and the observed auroral emission data. One possible reason for this timing difference is that the reconnection in the LFM global magnetospheric simulation is numerical, although the reconnection rate is related to the conditions external to the actual reconnection region. Therefore, reconnection related features such as substorm timing in the solar wind driver are possibly not well resolved by the simulation. However, this 10 min lag time is consistent with

the LFM substorm timing study performed by *Brogl et al.* [2009].

[43] Second, the simulated field-aligned Alfvénic Poynting flux might be underestimated in the event simulation. Numerical dissipation is one reason for this underestimation, which is associated with the particular numerical grid resolution. In the simulation, waves with frequency greater than 200 mHz are numerically damped in the plasma sheet region, which causes artificial dissipation of field-aligned AC Poynting flux. Another possible reason for the underestimation is the lack of kinetic physics in the single-fluid, ideal MHD simulation, since small-scale, dispersive Alfvén waves are not included in the LFM global simulation.

[44] However one views these differences, the degree of similarity in the observed and simulated temporal variation is informative and the LFM simulation suggests that the observed Alfvénic activity can originate from the magnetotail. The conditions driven by the environment data of Figure 3 result, in the simulation, in a band of Alfvénic Poynting flux in the auroral ionosphere with a 15 min periodicity, qualitatively similar to the observed variations in brightness in the keogram response to the soft electron precipitation of the event PBI. Thus we infer that it is reasonable to say that Alfvénic Poynting flux from tail reconnection can drive our event.

## 5.2. Alfvénic Signatures

[45] Detailed analysis of Alfvénic signatures observed in the electric and magnetic field will be described in a forthcoming paper (E. Lundberg et al., manuscript in preparation, 2012). There are clear, large-amplitude, dispersive Alfvén wave signatures associated with the field-aligned electrons. The electric field observations contain fluctuations in the 8 Hz range coincident with the electron precipitation. The DC electric fields indicate variable plasma drift velocities that reach 4 km/s. The measured ratio of  $\delta \mathbf{E}/\delta \mathbf{B}$  matches the theoretical Alfvén speed dependence on perpendicular wavelength (assuming that all measured variations are due to Doppler shift). The 8 Hz temporal modulation and Alfvénic signatures are reminiscent of reported auroral flickering observations [*Whiter et al.*, 2008; *Gustavsson et al.*, 2008], however no optical flickering could be observed in the ground-based data, possibly due to the oblique view.

[46] Figure 6 shows an enhanced view of the precipitation as seen by the main payload high-cadence field-aligned detector. Clear velocity dispersion signatures are evident. A simple time-of-flight analysis shows that acceleration by Alfvén waves must have ended only a few hundred km above the observation point. The Alfvén speeds calculated by the fields data are 1000–2000 km/s. Acceleration by linear and nonlinear wave-particle interactions between the ambient ionosphere and the dispersive Alfvén wave activity should accelerate the electrons up to twice the Alfvén speed along the field line [*Kletzing and Hu*, 2001; *Seyler*, 1990]; this corresponds to energies of only a few eV. The higher energy acceleration, observed up to 1 keV, must take place at higher altitudes where the Alfvén speed is higher. However, the observed electron dispersion signature is consistent with each burst of electrons leaving the acceleration region uniformly at a few hundred km above the payload (1000 to 1500 km altitude). Since the electron acceleration mechanisms require  $V_A \sim V_{the}$ , we might presume that the density

profile decreases rapidly above 1000 km. This is consistent with the scale height measurement for density from the two subpayloads HF wave observations. Note that steep gradients in  $V_A$  are required for Alfvén wave reflection [Knudsen *et al.*, 1992; Lysak, 1999] and therefore the rocket may be observing a fraction of the Alfvén wave power incident on the ionosphere.

### 5.3. Spatial Structuring as Tearing Mode Instability

[47] The camera data show that the rayed curtain has along-arc (zonal) structure with rays of 2 km width and 16 km spacing. In the in situ data, since the rays are moving across the observation point from the along-arc motion, this appears as a roughly 2 s intermittency in the energy flux. We interpret this spatial structuring in the context of theoretical and simulation investigations of the Kelvin-Helmholtz and tearing mode instabilities [Seyler, 1990; Chaston and Seki, 2010].

[48] We begin with reconnection in the tail sending a curtain of Alfvénic wave power down to the ionosphere, as described in the previous sections. As this activity approaches the dispersive ionosphere, it will develop a parallel electric field and a perpendicular wavelength. In a region of strong field-aligned current, this curtain of activity can develop an instability from the tearing mode. The models predict the growth of repeated spatial structuring in the along-arc direction with scale lengths of 1 to 1.3 times the width of the initial current sheet (C. C. Chaston, personal communication, 2012). If we consider the localized magnetic field distortion in Figure 7 as the relevant width (10 km) then indeed our 16 km spacing is thus consistent. The structure which develops means that the parallel electric field of the Alfvénic activity develops spatial structure along the arc, such that this  $E_{\parallel}$  is modulated from maximum to minimum and back every 16 km. This is consistent with the modulated brightness, and the modulated maximum electron energy, that we see every 16 km along the curtain.

### 5.4. Along-Arc Motion and Ionospheric Flows

[49] Finally we consider the along-arc motion of the resultant structures. The camera data see the observed enhancements moving in both directions along the arc at 8.5 km/s. This bidirectionality is interesting. The tearing mode instability, and its resulting along-arc structuring, has no inherent phase velocity along the arc; the only way to make the enhancements move is to embed them (at altitudes above their interaction between the  $E_{\parallel}$  and the electrons, where the dispersive development of the Alfvénic activity begins) in a DC electric field creating  $\mathbf{E} \times \mathbf{B}$  motion. (Note that this is a separate argument from other discussions of perpendicular phase velocity signatures observed *within* a ray; here we are discussing the motion of the rayed enhancements.)

[50] Mapping of this ionospheric structure to the tail using a Tsyganenko model says that 16 km structures would have an extent of  $0.2 R_E$  at the  $50 R_E$  position where the field lines intersect the equator. The 8 km/s motion would map to  $0.1 R_E/s$  across current sheet. However, it is difficult to propose a tail flow structure which is symmetric in the dawn-dusk and dusk-dawn directions. It is simpler to consider this motion as driven by ionospheric flow shears at the poleward auroral boundary, such as would be expected in an inverted-V system. The coherent, bidirectional motion is well matched

by the velocities corresponding to U-shaped potential structures. The observed velocity of 8.5 km/s, however, corresponds to an ionospheric electric field of a magnitude twice as large as the observed DC electric field structures. Thus we must infer the presence of a parallel potential drop between the observation point, and the evolving Alfvénic activity which is the source of the observed field-aligned electron precipitation. It is important to note, however, that there is clearly no signature of a magnetospheric or plasma sheet population being accelerated by such a parallel potential drop; the only electron precipitation observed at this time is clearly Alfvénic acceleration of an ionospheric population. Thus if such an inverted-V structure does exist above the observation point, as inferred by the motions of the structures, it is not in a location where it results in an accelerated plasma sheet electron beam; perhaps it is a newly reconnected lobe field line. It is interesting to consider the plausibility of such a structure: inverted-V potential structures are tightly tied to the local particle populations. Here the role of the inverted-V must involve quasi-neutrality through suppression of the ionospheric ion population rather than acceleration of a magnetospheric electron population.

[51] A question of interest for correlating the optical and in situ data is the relative location of the rays moving in opposite directions: do they move on separate coplanar curtains or are they essentially overlapping? In the U-shaped potential description just described, we are clearly inferring two closely spaced coplanar regions. Triangulation of individual rays in images from TOO and KAK is limited to  $\pm 5$  km due to the 0.5 s integration of the NCCD camera. Because the rays often dim significantly between brightening events the triangulated positions are generally only produced for the times when two rays coincide, which biases the measurement to the average of the position of the two rays. Comparing images from Toolik and Kaktovik, with the KAK keogram resampled to 0.5 s cadence, the intensifications occur at the same time, to within the 0.5 s resolution of the slower Toolik data. With a  $40^\circ$  separation in observing angle between KAK and TOO, this indicates that the intensifications are either temporal events, or the superposition of two individual rays traveling on different or intertwined curtains separated by not more than 10 km. The particle data show significant precipitation for nearly 30 s, however only for the first 10 to 15 s is the energy flux sufficient to produce observable rays, which is comparable to the dimensions determined from the parallax argument above. The flux beyond  $T + 615$  s would produce dimmer, higher average altitude rays at the limit of detectability that contribute to an overall haze seen in some of the KAK images. Thus, the camera data are consistent with a picture requiring nearby, but not overlapping, coplanar sheets of rays with opposing along-arc motions.

[52] Using the high temporal resolution data we have quantified along-arc motion of rays within the poleward boundary arc moving at  $8.5 \pm 0.5$  km/s in either direction and with an average spacing between rays of  $16 \pm 2.8$  km, with individual ray sizes ranging from 1 to 4.5 km. Under what conditions this type of activity is found cannot be determined from this single experiment, but our optical observations from subsequent nights have shown similar morphology and dynamics differences between the most poleward and adjacent arcs, indicating that the Cascades2

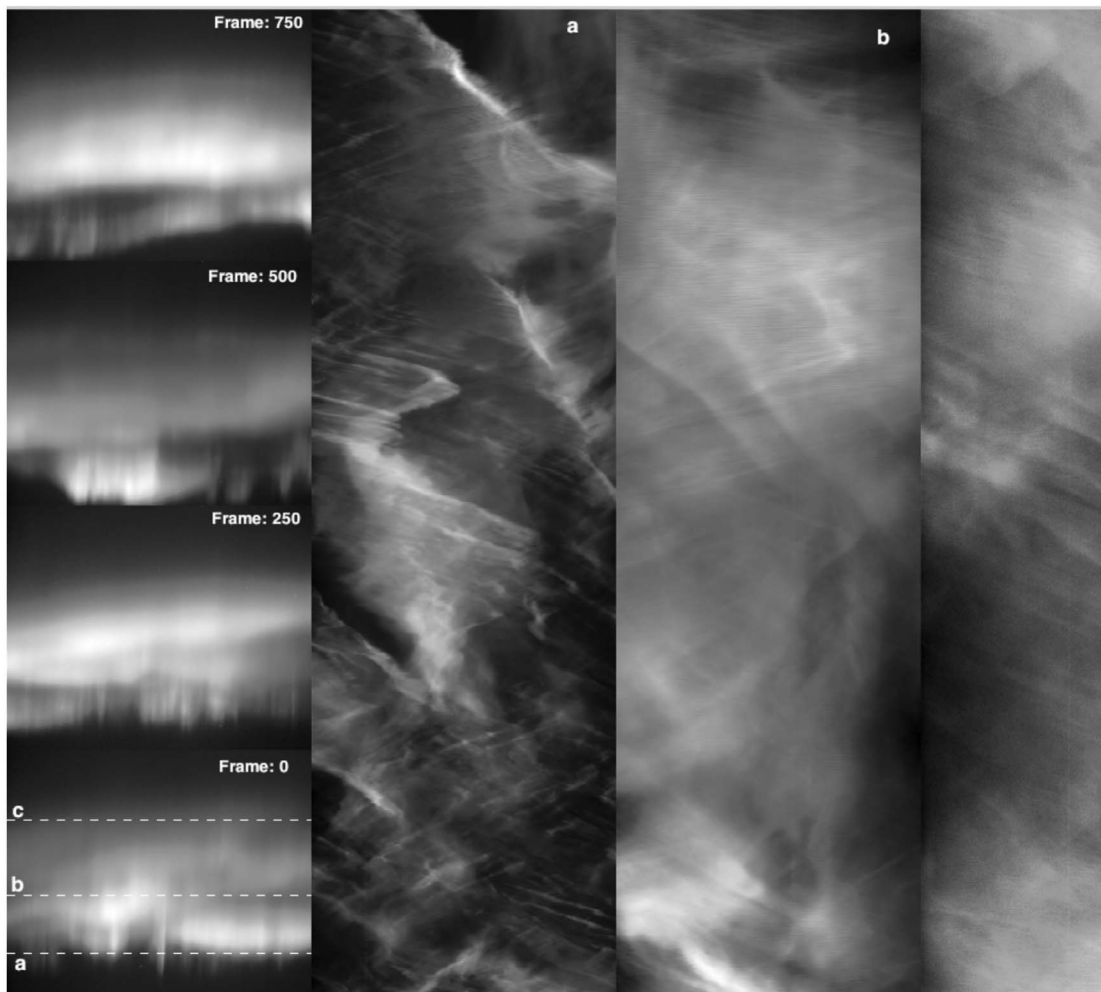


**Figure 12.** Another PBI keogram example, from 2 February 2010, a 30 s interval beginning at 09:04:55 UT. In the first panel, four frames from the sequence, labeled by frame number. The second to fourth panels show three keograms at three altitudes as labeled in the left frame. The lowest altitude, farthest poleward signature shows similar bidirectional motion of periodic structures as in our case study event from March 2009.

observations are not a unique event. Figure 12 shows another example of keograms created from narrow field camera views of another PBI event, from 2 February 2010 at 09:00 UT. It shows similar diagonal structuring indicative of motion of regular-spaced rays moving in both directions along the curtain.

## 6. Conclusions and Open Questions

[53] The entire poleward rayed arc observed in the KAK all-sky may encompass a single bead-like intensification as described by *Zesta et al.* [2006]. We interpret the finer structure within this event in the following manner. The source of the driving energy is reconnection in the tail sending Alfvénic Poynting flux to the poleward boundary region of the nightside ionosphere. The resulting curtain of Alfvénic activity becomes dispersive in the inhomogeneous ionosphere (that is, it develops a  $k_{\perp}$  and an  $E_{\parallel}$ ) and accelerates ionospheric electrons into the atmosphere from low altitudes. This Alfvénic activity, and the resulting electron

acceleration, is modulated along the length of the curtain by a tearing mode instability, causing enhancements in  $\mathbf{E}_{\parallel}$  and the resulting maximum electron acceleration energy and auroral brightness with spatial scales of 16 km along the arc. This Alfvénic activity is entrained in ionospheric DC electric structures of a U-shaped potential form, causing the visible rays and the electron bursts to move in both directions along the arc at velocities of 8.5 km/s. This DC electric field structure must also include a region of inverted-V  $E_{\parallel}$ , but this potential drop, while below the altitude where the  $k_{\perp}$  and  $\mathbf{E}_{\parallel}$  of the Alfvénic activity become modulated, must be above the altitude of significant electrons to be accelerated by it.

[54] The interpretation of the visible rayed structures along the curtain as caused by an along-arc modulation of the maximum energy of interaction between the Alfvén waves and the ionospheric electrons is different from two typical explanations of such rays. These typical explanations, compared by *Ivchenko et al.* [2005], are that (1) each ray is a stand-alone tube of Alfvénic activity or (2) that the rays are

caused by looking sideways through a folded curtain structure. The Cascades2 observations are not consistent with explanation 1 because the electron precipitation does not cease between the rays, it is only lower in maximum energy. They are not consistent with explanation 2 because the observed rays are seen to move bidirectionally. Instead, we consider the rayed curtain and its motion as a combination of Alfvénic and quasi-static U-shaped potential activity. Other recent studies [Dahlgren et al., 2010; Asamura et al., 2009] have also begun to explore these interesting combinations of quasi-static and Alfvénic activity.

[55] Open questions not addressed by this data set are as follows. (1) What exactly is the interaction between the Alfvénic wave activity and the larger-scale ionospheric flows and fields, and what role does this interaction play in the coupled MI system? (2) What causes the localization of the current sheet enhancement within the larger-scale current sheet? (3) By what particular mechanism does the tail reconnection produce the observed Alfvénic Poynting flux? Recent 3-D reconnection studies [Shay et al., 2011] show that in addition to the Poynting flux generated by the braking of earthward ion flows (as modeled in the LFM model here), there is also directly produced kinetic Alfvén wave power. It is interesting to consider whether this KAW activity maps directly to the poleward curtain PBI activity, while the ion flows and their braking-produced Alfvénic activity maps to PBI streamers.

[56] **Acknowledgments.** The authors thank both reviewers for their thoughtful and constructive commentary. The authors wish to thank Dave Knudsen (Calgary), Josh Semeter (BU), Chris Chaston (UCB), Bob Lysak (Minnesota) and Barrett Rogers (DC) for useful conversations. Dartmouth undergraduate researcher Ben Feintzeig reduced the magnetometer data. The Cascades2 science team thanks their engineering staff and the personnel at WFF/NSROC, PFRR, and PFISR. The Cascades2 program was funded by the NASA/LCAS program and administered by the WFF/SRPO.

[57] Robert Lysak thanks the reviewers for their assistance in evaluating this paper.

## References

- Angelopoulos, V. (2008), The THEMIS mission, *Space Sci. Rev.*, *141*, 5, doi:10.1007/s11214-008-9336-1.
- Angelopoulos, V., J. A. Chapman, F. S. Mozer, J. D. Scudder, C. T. Russell, K. Tsuruda, T. Mukai, T. J. Hughes, and K. Yumoto (2002), Plasma sheet electromagnetic power generation and its dissipation along auroral field lines, *J. Geophys. Res.*, *107*(A8), 1181, doi:10.1029/2001JA900136.
- Arnoldy, R. L., K. A. Lynch, and J. B. Austin (1999), Energy and pitch angle dispersed auroral electrons suggesting a time-variable, inverted-V potential structure, *J. Geophys. Res.*, *104*, 22,613.
- Asamura, K., et al. (2009), Sheared flows and small-scale Alfvén wave generation in the auroral acceleration region, *Geophys. Res. Lett.*, *36*, L05105, doi:10.1029/2008GL036803.
- Borovsky, J. E. (1993), Auroral arc thicknesses as predicted by various theories, *J. Geophys. Res.*, *98*, 6101.
- Brogl, S., R. E. Lopez, M. Wiltberger, and H. K. Rassoul (2009), Studies of magnetotail dynamics and energy evolution during substorms using MHD simulations, *Ann. Geophys.*, *27*(4), 1717–1727, doi:10.5194/angeo-27-1717-2009.
- Carlson, C. W., D. W. Curtis, G. Paschmann, and W. Michael (1983), An instrument for rapidly measuring plasma distribution functions with high resolution, *Adv. Space Res.*, *2*, 67.
- Chaston, C. C., and K. Seki (2010), Small-scale auroral current sheet structuring, *J. Geophys. Res.*, *115*, A11221, doi:10.1029/2010JA015536.
- Chaston, C. C., L. M. Peticolas, J. W. Bonnell, C. W. Carlson, R. E. Ergun, J. P. McFadden, and R. J. Strangeway (2003), Width and brightness of auroral arcs driven by inertial Alfvén waves, *J. Geophys. Res.*, *108*(A2), 1091, doi:10.1029/2001JA007537.
- Chaston, C. C., K. Seki, T. Sakanoi, K. Asamura, and M. Hirahara (2010), Motion of aurorae, *Geophys. Res. Lett.*, *37*, L08104, doi:10.1029/2009GL042117.
- Chaston, C. C., K. Seki, T. Sakanoi, K. Asamura, M. Hirahara, and C. W. Carlson (2011), Cross-scale coupling in the auroral acceleration region, *Geophys. Res. Lett.*, *38*, L20101, doi:10.1029/2011GL049185.
- Clemmons, J. H., C. W. Carlson, and M. H. Boehm (1995), Impulsive ion injections in the morning auroral region, *J. Geophys. Res.*, *100*, 12,133.
- Dahlgren, H., A. Aikio, K. Kaila, N. Ivchenko, B. Lanchester, D. Whiter, and G. Marklund (2010), Simultaneous observations of small multi-scale structures in an auroral arc, *J. Atmos. Sol. Terr. Phys.*, *72*, 633.
- Frissell, N. A., J. B. H. Baker, J. M. Ruohoniemi, L. B. N. Clausen, Z. C. Kale, I. J. Rae, L. Kepko, K. Oksavik, R. A. Greenwald, and M. L. West (2011), First radar observations in the vicinity of the plasmopause of pulsed ionospheric flows generated by bursty bulk flows, *Geophys. Res. Lett.*, *38*, L01103, doi:10.1029/2010GL045857.
- Gustavsson, B., J. Lunde, and E. M. Blixt (2008), Optical observations of flickering aurora and its spatiotemporal characteristics, *J. Geophys. Res.*, *113*, A12317, doi:10.1029/2008JA013515.
- Hui, C., and C. E. Seyler (1992), Electron acceleration by alfvén waves in the magnetosphere, *J. Geophys. Res.*, *97*, 3953.
- Ivchenko, N., G. Marklund, K. Lynch, D. Pietrowski, R. Torbert, F. Primdahl, and A. Ranta (1999), Quasiperiodic oscillations observed at the edge of an auroral arc by Auroral Turbulence II, *Geophys. Res. Lett.*, *26*, 3365.
- Ivchenko, N., E. M. Blixt, and B. S. Lanchester (2005), Multispectral observations of auroral rays and curls, *Geophys. Res. Lett.*, *32*, L18106, doi:10.1029/2005GL022650.
- Jones, S. L., et al. (2008), PFISR and ROPA observations of pulsating aurora, *J. Atmos. Sol. Terr. Phys.*, *71*, 708, doi:10.1016/j.jastp.2008.10.004.
- Keiling, A., et al. (2008), Multiple intensifications inside the auroral bulge and their association with plasma sheet activities, *J. Geophys. Res.*, *113*, A12216, doi:10.1029/2008JA013383.
- Kletzing, C. A. (1994), Electron acceleration by kinetic Alfvén waves, *J. Geophys. Res.*, *99*, 11,095.
- Kletzing, C. A., and S. Hu (2001), Alfvén wave generated electron time dispersion, *Geophys. Res. Lett.*, *28*, 693.
- Knudsen, D. J., M. C. Kelley, and J. F. Vickrey (1992), Alfvén waves in the auroral ionosphere: A numerical model compared with measurements, *J. Geophys. Res.*, *97*, 77.
- Lummerzheim, D., and J. Liliensten (1994), Electron transport and energy degradation in the ionosphere: Evaluation of the numerical solution, comparison with laboratory experiments and auroral observations, *Ann. Geophys.*, *12*, 1039.
- Lundberg, E. T., P. M. Kintner, K. A. Lynch, and M. R. Mella (2012a), Multipayload measurement of transverse velocity shears in the topside ionosphere, *Geophys. Res. Lett.*, *39*, L01107, doi:10.1029/2011GL050018.
- Lundberg, E. T., P. M. Kintner, S. P. Powell, and K. A. Lynch (2012b), Multipayload interferometric wave vector determination of auroral hiss, *J. Geophys. Res.*, *117*, A02306, doi:10.1029/2011JA017037.
- Lynch, K. A., D. Pietrowski, R. B. Torbert, N. Ivchenko, G. Marklund, and F. Primdahl (1999), Multiple-point electron measurements in a nightside auroral arc: Auroral Turbulence II particle observations, *Geophys. Res. Lett.*, *26*, 3361.
- Lynch, K. A., J. L. Semeter, M. Zettergren, P. Kintner, R. Arnoldy, E. Klatt, J. LaBelle, R. Michell, E. MacDonald, and M. Samara (2007), Auroral ion outflow: Low altitude energization, *Ann. Geophys.*, *25*, 1967.
- Lyon, J., J. Fedder, and C. Mobarly (2004), The Lyon Fedder Mobarly (LFM) global MHD magnetospheric simulation code, *J. Atmos. Sol. Terr. Phys.*, *66*(15–16), 1333, doi:10.1016/j.jastp.2004.03.020.
- Lyons, L., T. Nagai, G. T. Blanchard, J. C. Samson, T. Yamamoto, T. Mukai, A. Nishida, and S. Kokubun (1999), Association between GEOTAIL plasma flows and auroral poleward boundary intensifications observed by CANOPUS photometers, *J. Geophys. Res.*, *104*, 4485.
- Lysak, R. L. (1999), Propagation of Alfvén waves through the ionosphere: Dependence on ionospheric parameters, *J. Geophys. Res.*, *104*, 10,017.
- Lysak, R. L., and Y. Song (2005), Nonlocal interactions between electrons and Alfvén waves on auroral field lines, *J. Geophys. Res.*, *110*, A10S06, doi:10.1029/2004JA010803.
- Mella, M. R., K. A. Lynch, D. L. Hampton, H. Dahlgren, P. M. Kintner, M. Lessard, D. Lummerzheim, E. T. Lundberg, M. J. Nicolls, and H. C. Stenbaek-Nielsen (2011), Sounding rocket study of two sequential auroral poleward boundary intensifications, *J. Geophys. Res.*, *116*, A00K18, doi:10.1029/2011JA016428.
- Newell, P. T., T. Sotirelis, and S. Wing (2009), Diffuse, monoenergetic, and broadband aurora: The global precipitation budget, *J. Geophys. Res.*, *114*, A09207, doi:10.1029/2009JA014326.
- Obuchi, Y., T. Sakanoi, K. Asamura, A. Yamazaki, Y. Kasaba, M. Hirahara, Y. Ebihara, and S. Okano (2011), Fine-scale dynamics of black auroras obtained from simultaneous imaging and particle observations with the Reimei satellite, *J. Geophys. Res.*, *116*, A00K07, doi:10.1029/2010JA016321.

- Partamies, N., M. Syrjasuo, E. Donovan, M. Connors, D. Charrois, D. Knudsen, and Z. Kryzanowsky (2010), Observations of the auroral width spectrum at kilometre-scale size, *Ann. Geophys.*, *29*, 711.
- Paschmann, G., S. Haaland, and R. Treumann (Eds.) (2003), *Auroral Plasma Physics, Space Sci. Ser. ISSI*, vol. 15, Kluwer Acad., Dordrecht, Netherlands.
- Rae, I. J., C. E. J. Watt, I. R. Mann, K. R. Murphy, J. C. Samson, K. Kabin, and V. Angelopoulos (2010), Optical characterization of the growth and spatial structure of a substorm onset arc, *J. Geophys. Res.*, *115*, A10222, doi:10.1029/2010JA015376.
- Samara, M., R. G. Michell, K. Asamura, M. Hirahara, D. L. Hampton, and H. C. Stenback-Nielsen (2010), Ground-based observations of diffuse auroral structures in conjunction with Reimei measurements, *Ann. Geophys.*, *28*(3), 873, doi:10.5194/angeo-28-873-2010.
- Semeter, J., C. J. Heinselman, G. G. Sivjee, H. U. Frey, and J. W. Bonnell (2005), Ionospheric response to wave-accelerated electrons at the poleward auroral boundary, *J. Geophys. Res.*, *110*, A11310, doi:10.1029/2005JA011226.
- Seyler, C. E. (1988), Nonlinear 3-D evolution of bounded kinetic Alfvén waves due to shear flow and collisionless tearing instability, *Geophys. Res. Lett.*, *15*, 756.
- Seyler, C. E. (1990), A mathematical model of the structure and evolution of small-scale discrete auroral arcs, *J. Geophys. Res.*, *95*, 17,199.
- Seyler, C. E., and K. Liu (2007), Particle energization by oblique inertial Alfvén waves in the auroral region, *J. Geophys. Res.*, *112*, A09302, doi:10.1029/2007JA012412.
- Shay, M. A., J. F. Drake, J. P. Eastwood, and T. D. Phan (2011), Super-Alfvénic propagation of substorm reconnection signatures and poynting flux, *Phys. Rev. Lett.*, *107*, 065001, 10.1103/PhysRevLett.107.065001.
- Stenback-Nielsen, H. C., T. J. Hallinan, D. L. Osborne, J. Kimball, C. Chaston, J. McFadden, G. Delory, M. Temerin, and C. W. Carlson (1998), Aircraft observations conjugate to FAST auroral arc thicknesses, *Geophys. Res. Lett.*, *25*, 2073.
- Trondsen, T. S., and L. L. Cogger (1998), A survey of small-scale spatially periodic distortions of auroral forms, *J. Geophys. Res.*, *103*, 9405.
- Watt, C. E. J., R. Rankin, I. J. Rae, and D. M. Wright (2005), Self-consistent electron acceleration due to inertial Alfvén wave pulses, *J. Geophys. Res.*, *110*, A10S07, doi:10.1029/2004JA010877.
- Whiter, D. K., B. S. Lanchester, B. Gustavsson, N. Ivchenko, J. M. Sullivan, and H. Dahlgren (2008), Small-scale structures in flickering aurora, *Geophys. Res. Lett.*, *35*, L23103, doi:10.1029/2008GL036134.
- Wu, K., and C. E. Seyler (2003), Instability of inertial Alfvén waves in transverse sheared flow, *J. Geophys. Res.*, *108*(A6), 1236, doi:10.1029/2002JA009631.
- Wygant, J. R., et al. (2000), Polar spacecraft based comparisons of intense electric fields and Poynting flux near and within the plasma sheet-tail lobe boundary to UVI images: An energy source for the aurora, *J. Geophys. Res.*, *105*, 18,675.
- Zesta, E., E. Donovan, L. Lyons, G. Enno, J. S. Murphree, and L. Cogger (2002), Two-dimensional structure of auroral poleward boundary intensifications, *J. Geophys. Res.*, *107*(A11), 1350, doi:10.1029/2001JA000260.
- Zesta, E., L. Lyons, C.-P. Wang, E. Donovan, H. Frey, and T. Nagai (2006), Auroral poleward boundary intensifications (PBIs): Their two-dimensional structure and associated dynamics in the plasma sheet, *J. Geophys. Res.*, *111*, A05201, doi:10.1029/2004JA010640.
- Zettergren, M., J. Semeter, B. Burnett, W. Oliver, C. Heinselman, P.-L. Blelly, and M. Diaz (2010), Dynamic variability in f-region ionospheric composition at auroral arc boundaries, *Ann. Geophys.*, *28*(2), 651, doi:10.5194/angeo-28-651-2010.
- Zhang, B., W. Lotko, O. Brambles, P. Damiano, M. Wiltberger, and J. Lyon (2012), Magnetotail origins of auroral Alfvénic power, *J. Geophys. Res.*, *117*, A09205, doi:10.1029/2012JA017680.
- Zou, S., L. R. Lyons, M. J. Nicolls, C. J. Heinselman, and S. B. Mende (2009), Nightside ionospheric electrodynamic associated with substorms: PFISR and THEMIS ASI observations, *J. Geophys. Res.*, *114*, A12301, doi:10.1029/2009JA014259.